Recordings of the Parkfield 2004 Earthquake on the GEOS Array: Implications for Earthquake Precursors, Fault Rupture, and Co-Seismic Strain Changes

Roger D. Borcherdt, Malcolm J.S. Johnston, Gary Glassmoyer, and Christopher Dietel

U.S. Geological Survey, Menlo Park, CA

Bulletin Seismological Society of America

Special Issue Parkfield 2004 Earthquake

Submitted: September 22, 2005

Revised: January 26, 2006

Accepted March 6, 2006

Recordings of the Parkfield 2004 Earthquake on the GEOS Array: Implications for Earthquake Precursors, Fault Rupture, and Co-Seismic Strain Changes

Roger D. Borcherdt, Malcolm J.S. Johnston, Gary Glassmoyer, and Christopher Dietel

U.S. Geological Survey, Menlo Park, CA

ABSTRACT

The 2004 Parkfield earthquake generated a unique set of near-field, high-resolution co-located measurements of acceleration, volumetric strain, and velocity at 11 stations in the GEOS (General Earthquake Observation System) Array. The recordings indicate no precursory strain or displacement was discernable at sensitivities of 10^{-11} strain and $5x10^{-8}$ meters 25 seconds prior to the earthquake at distances of 0.5 to 12 km from the fault rupture. Coherent fault-parallel and fault-normal displacement pulses, observed along the fault north of the epicenter, are consistent with model predictions for "fling", directivity, and displacement for right-lateral, strike-slip, fault rupture. The fault-parallel and fault-normal pulses imply apparent rupture velocities of 2.86 ± 0.15 and 3.03 ± 0.24 km/sec, respectively. Unprecedented high-resolution volumetric-strain recordings on opposite sides of the fault show that dynamic strains radiated from ruptured segments of the fault are more than an order of magnitude larger than final coseismic strain offsets associated with fault slip, suggesting that dynamic radiated strain may have contributed to the triggering of failure on unruptured segments. High-resolution recordings show that coseismic strain offsets occur abruptly over time intervals of less than 10 seconds near the time of arrival of the dominant radiated fault-parallel and fault-normal displacements. Subsequent measurements show that the strain offsets continue to increase by as much as 69 percent in 5 minutes and 300 percent in 24 hours over that measured during initial fault slip at depth. Estimates of local material parameters from simultaneous measurements of volumetric strain and acceleration confirm seismic calibration factors previously measurable in-situ only at tidal periods.

INTRODUCTION

The suggested occurrence of a repeat moderate M ~ 6.0 earthquake on the San Andreas Fault near Parkfield, CA (Bakun and McEvilly, 1984; Bakun and Lindh, 1985) stimulated the design and installation of several experiments in the area. The GEOS Array was designed to address a variety of near-source scientific and engineering issues. The array was configured

to provide high resolution, broad-band, on-scale, near-source digital recordings of crustal failure processes and resultant seismic radiation fields using co-located accelerometers, velocity transducers, and volumetric strain sensors (Borcherdt and Johnston, 1988). The array uses an effective recording dynamic range available up to 180 dB to provide recordings of signals ranging in amplitude from seismic background noise level as detected by velocity transducers and dilatometers to strong motions and strains near the fault rupture surface as detected by accelerometers and dilatometers. Installation of the array was completed by 1987 along the section of the fault that was expected to rupture by 1993.

The Parkfield earthquake of September 28, 2004 occurred along the same segment of the San Andreas Fault that ruptured, albeit in the opposite direction, during the 1966 Parkfield earthquake (Rymer *et al*., this volume; Langbein *et al*., 2005). As a result the earthquake generated a unique set of high-resolution measurements of acceleration and volumetric strain in the near-source region. In addition to the recordings on the GEOS Array the earthquake generated an extensive set of near-source strong-motion recordings on 38 analog and 2 digital stations operated by the California Geological Survey (CGS) Strong-Motion Instrumentation Program (Shakal *et al*., 2005; http://www.quake.ca.gov/cisn-edc/). The combined set of recordings provides a set of on-scale measurements at an unprecedented geographic resolution in the near-source region of a M 6 earthquake.

This paper briefly describes the GEOS Array and the corresponding high resolution recordings of acceleration, velocity, and volumetric strain. It evaluates the high gain recordings of volumetric strain and velocity for the potential existence of precursory signals. It utilizes the GEOS accelerometer and dilatometer recordings together with the CGS accelerometer recordings for sites on both sides of the fault to infer the nature of fault rupture propagation. The high resolution GEOS recordings document the nature of radiated dynamic strain variations and co-seismic static offsets in strain that occur over time intervals of 10 seconds as slip on the segment of the fault nearest the site occurs. Implications of the high-resolution co-located measurements for post-seismic strain changes, rupture propagation, local material properties, and sensor calibration are presented.

ARRAY DESIGN

The GEOS array near Parkfield, CA is comprised of eleven stations, distributed at distances ranging from 0.5 to 10 km along both sides of the San Andreas Fault zone (Figure 1). All of the stations are equipped with co-located three-component accelerometers (FBA 13, natural frequency 100 Hz, ± 2g full scale) and velocity transducers (natural frequency 1 or 2 Hz). Five of the stations are equipped with borehole volumetric strain meters (Johnston *et al*., 1982, this volume).

The signals from the sensors at each site are recorded on site at 200 samples per second using a six channel, portable, low-power (< 2 watts quiescent), digital recorder (General Earthquake Observation System, GEOS; Borcherdt *et al*., 1985). The signals from the dilatometers also are transmitted and recorded via GOES satellite at one sample per 10 minutes (Johnston *et al*., 1982; Johnston *et al*., this volume). The portable digital GEOS recorders record signals between ± 10 volt in either AC or DC coupled modes with up to 84 dB gain in 6 dB steps at 16 bit (96 dB) resolution for a maximum dynamic range without

operator intervention at 1 second near 180 dB. The GEOS recorders in the array were programmed to record seismic signals over a dynamic range of about 130 dB and over a bandwidth of about 15 to 0.02 seconds (0.06 to 50 Hz) depending on the strength of the input signal. Signals from the dilatometers were initially programmed to be recorded on the GEOS at two gain levels, separated by 30 dB, in both AC and DC coupled modes. The lower limit of resolution for acceleration is near 6×10^{-6} g and that for volumetric strain near 10^{-11} strain. The GEOS recording systems are programmed to trigger on events with M > 3 anywhere in the rupture zone in order to minimize maintenance visits and consumption of power provided by batteries and solar cells. Sensor and recording system calibrations are recorded with each storage media change, the frequency of which varied between 3 and 12 months.

Previous examples of dilatometer recordings at other locations, their interpretation, and the theoretical framework for interpretation of co-located seismometer measurements are presented in Johnston *et al.* (1982; 1984; 1986; 1987a; 1987b; 2002) and Borcherdt *et al*., (1985; 1988a; 1988b; 1989).

The original three-component acceleration and volumetric-strain time histories recorded on the GEOS recorders for the Parkfield 2004 earthquake are shown superimposed on a station map in Figure 1. Seventeen seconds of time history are shown, starting 2 seconds before the P arrival. Recordings of velocity transducers at the sites are not shown. Comparison of the traces shows considerable variation in amplitude and frequency content depending on the site's location. The largest peak acceleration observed on the array was 609 cm/sec^2 at the Joaquin Canyon site (see Borcherdt *et al.*, 2004 for detailed description of data set). Events recorded on the array during the preceding 20 years and the subsequent aftershocks are available via the internet (http://nsmp.wr.usgs.gov/GEOS/geos.html).

HIGH-RESOLUTION PRE-EVENT DISPLACEMENT AND VOLUMETRIC STRAIN MEASUREMENTS

Displacement time histories inferred from the vertical component of velocity recorded at each site are shown in Figures 2a and 2b. Corresponding volumetric strain time histories are shown in Figure 2c. The time histories are shown for 25 or 2.3 second intervals prior to the arrival of the first P wave energy depending on the length of the pre-event buffer chosen by the operator for the recorder. The value of the maximum amplitude prior to the arrival of the P wave is shown for each pre-event time history.

Neither the displacement nor strain pre-event time histories recorded at 200 sps (Figure 2) show a signal recognized (Johnston *et al*., this volume) as a precursory signal prior to the arrival of the P wave energy. The value of the maximum amplitude shown for each trace indicates that if a precursory signal exists then its amplitude must be less than the maximum observed values of 0.15 nanostrain and 0.5 nanometers. The accelerometers and dilatometers closest to the hypocenter are those at the Gold Hill and Froelich sites. The Gold Hill accelerometer is within 3 km of the epicenter and about 8 km of the hypocenter. The Froelich site is at a hypocentral distance of about 17 km and about 2 km from the fault rupture. The lack of precursory signals at these sites and the high sensitivities of 10^{-11} strain and 10^{-10} m displacements as indicated in the recordings (Figure 2) suggests that if precursory signals are

to be detected then the sensors will need to be significantly closer to the nucleation source zone. A detailed discussion of this recorded result in relation to model and laboratory results and their implications for earthquake prediction are provided by (Johnston *et al*., this volume).

IMPLICATIONS OF RECORDED ACCELERATIONS FOR FAULT RUPTURE

The proximity of a number of strong-motion recording locations to the fault-rupture surface provides a unique opportunity to examine characteristics of the motions radiated by nucleation and propagation of fault rupture. The relatively uniform geographic distribution of stations along the fault north of the epicenter is especially useful in this regard.

To develop a spatial image of the dynamic displacements along the northern section of the fault, displacement time histories inferred in the fault-parallel ($N322^0E$) and the fault-normal ($N052^0E$) directions are superimposed on a map showing the San Andreas fault, surface fractures mapped following the Parkfield 2004 earthquake, and the locations of the strong-motion recording stations (Figures 3, 4, and 5). The displacement time histories are arranged with a common origin time extending to the right for sites on the east side of the fault and to the left for sites on the west side of the fault. The time histories are plotted with the same amplitude scale. The displacement time histories were derived by double integration of the acceleration time histories filtered with a low-cut, 20 second, non-causal, two-pole Butterworth filter. Time histories are shown only for GEOS and CGS sites (Shakal *et al*., 2005) closest to the surface projection of the fault rupture north of the epicenter. Inspection of these time histories arranged according to location with respect to the fault rupture reveals several interesting aspects of the motions.

Coherent and distinctive displacement pulses are apparent in the record sections for the fault-parallel and fault-normal motions on both sides of the fault (Figures 3 and 4). The coherency of the pulses for horizontal motion is most evident for sites a few kilometers north of the epicenter or north of station FZ4. A coherent upward pulse of vertical motion (Figure 5) is apparent for the sites on the east side of the fault, but none is apparent for corresponding sites on the west side of the fault.

The fault-parallel record sections (Figure 3) show that the first motion for sites north of site FZ6 is positive for sites on the west side of the fault and negative for sites on the east side, indicative of right-lateral fault slip. This initial motion is followed by a well-defined negative trough for sites on the west side of the fault and a positive peak for sites on the east side. With the exception of FZ14, the amplitudes of the fault-parallel displacements are similar for sites on both sides of the fault with those on the west side of the fault and north of the EFU site being slightly larger.

The fault-normal motions (Figure 4) show a dominant coherent displacement pulse that is largest for sites north of FZ6. The initial coherent positive pulse is in the positive $N052^0E$ direction for the sites on both sides of the fault. This initial pulse is followed by a large dominant negative pulse in the $N232^0E$ direction. This coherent displacement pulse for sites north of the epicenter indicates that during the arrival of the pulse, sites on both sides of the fault moved in the same direction in contrast to the first pulse of fault-parallel motion during which the first motions were in opposite directions. The amplitudes of the fault-normal displacements along the northern section of the fault are significantly larger than the fault-

parallel and vertical displacements. This difference in the amplitude of the horizontal motions helps confirm earlier observations of this difference for other earthquakes. It provides additional evidence that may be an important consideration in the development of ground motion estimates for the site-specific, earthquake-resistant design of some structures (Somerville *et al*., 2000).

The vertical record sections (Figure 5) show that the initial displacement is downward followed by a coherent upward pulse at sites FZ14, FZ15, and VC1W on the west side of the fault and each of the sites on the east side. Coherent pulses are not apparent for the other sites on the west side of the fault especially for sites in the vicinity of the epicenter. The maximum vertical amplitudes are comparable for sites on the east side of the fault, north of and including FZ8, and for sites FZ14 and FZ15 near the fault, suggesting a relatively coherent vertical motion of the area northeast of the fault. No such coherency exists for the area west of the fault and south of FZ14. The large pulses of horizontal displacement apparent at the FZ14 site are distinctively larger than those at nearby sites of FZ9 and FFU on the west side of the fault. The large amplitudes at this site may be indicative of both source rupture characteristics and local site amplification characteristics. Large amplitudes at this site, which is located near the northern end of the southwest fracture zone, are consistent with rupture propagating northward but terminating near this location. Additional surface fractures as mapped by Rymer *et al*. (this volume) are also consistent with larger motions at this site. Liu *et al*., (this volume) developed estimates of local site response for CGS sites using recordings of the Coalinga earthquake. They indicate that the recordings obtained at sites FZ12, FZ14, and FZ1 are influenced by local site amplification effects.

Comparison of the displacement amplitudes at pairs of sites (FZ7, FZ8), (EFU, FZ11) and (VC1W, VC2W) shows that the maximum fault-parallel and fault-normal displacements attenuate with perpendicular distance from the fault rupture as opposed to distance from the hypocenter (see Figures 3 and 4). This observation suggests that the sources of the dominant pulses observed in the fault-parallel and fault-normal directions are located on the fault rupture surface. Their timing indicates that they are the radiation field resulting from the passage of the main rupture front at depth. A corresponding comparison for vertical motion shows that the pulses do not attenuate in similar fashion, suggesting that the vertical amplitudes may also be due in part to the development of surface waves.

The model of a strike-slip fault as formulated by Hisada and Bielak (2003) provides insight into the observed motions. Their model provides a theoretical formulation of the representation theorem which allows the static and dynamic components of the fault-parallel and fault-normal motions to be computed efficiently. Their results provide a physical interpretation of fling and directivity associated with various fault models. Their results presented for a strike-slip fault which extends to the surface in a uniform half-space are appropriate for consideration here. The model predictions, although not yet completed for a layered model corresponding to the crustal structure near Parkfield, are useful for understanding the general nature of the observed motions. Calculations for a half-space model with rupture velocity $v_r = 2.5$ km/secs, density $\rho = 2.5$ g/cm^3, wave speed for homogenous P and S waves $v_{HP} = 5$ km/sec and $v_{HS} = 3$ km/sec, and quality factors for homogeneous P and S waves of $Q_{HP} = 200$, and $Q_{HS} = 100$ are shown in figures 11a , 12c, and 12d of Hisada and Bielak (2003).

Fault-normal motions as predicted by the model (Hisada and Bielak, 2003) increase in the forward direction of the rupture front. This theoretically predicted directivity effect is apparent as a coherent fault-normal displacement pulse that is well developed at a distance of about 25% of the rupture length. Their model predicts the fault-normal displacements are dominated by the contributions from the dynamic terms of the solution with those from the static displacement offset being small and attenuating rapidly away from the fault. These general theoretical results for a simple strike-slip model are consistent with those observed (see Figure 4). The fault-normal static offsets are difficult to infer from the recorded accelerometer signals for the Parkfield earthquake, because the accelerometers lack sensitivity to long-period motion.

Fault-parallel displacements, termed "fling", as predicted by the model of Hisada and Bielak (2003) are dominated by the contributions of the fault-parallel static-offset terms. Their model predicts that the fault-parallel displacement at sites on the two sides of the fault should be in opposite right-lateral directions. Their results indicate that the contributions of the dynamic terms to the fault-normal displacements are greater than those to the fault-parallel displacements. These results are consistent with those observed (see Figures 3 and 4), although the observed displacements show evidence of additional seismic radiation. These fault-parallel static offsets are not readily inferred from the observed data, again because of the lack of long-period sensitivity of the accelerometers.

Travel times for coherent pulses of fault-parallel and fault-normal displacements are plotted as a function of hypocentral distance in Figures 6a and 6b. Travel times for the fault-parallel motion (Figure 6a) are the times of the first positive peak in displacement for sites west of the fault and the first negative peak for sites east of the fault. The travel times for the fault-normal motion (Figure 6b) are the times of the first positive peak for sites on west and east side of the fault. The origin time for the plots coincides with that of the earthquake.

Linear least squares regression curves fit to the travel times for the fault-parallel and the fault-normal data sets are shown in Figures 6a and 6b together with the 95 percent confidence limits on the ordinate and the 2 standard error of the estimate limits. The regression curves indicate an average apparent rupture velocity as apparent at the surface for the section of the fault north of the epicenter of about 2.86 ± 0.15 km/sec (Figure 6a) for the fault-parallel arrivals and 3.03 ± 0.24 km/sec (Figure 6b) for the fault-normal arrivals (uncertainty for each estimate is specified as one standard error of the regression coefficient). To test the null hypotheses that the true population regression coefficients for the two sets of travel times are equal, the sample regression coefficients, v_1 and v_2 for the two samples are used to calculate the t statistic defined by $t = |(v_1 - v_2)/\sqrt{s_{v_1}^{\ 2} + s_{v_2}^{\ 2}}|$. Comparison of t with theoretical values at various significance levels for a sample size of $n_1 + n_2 - 4 = 28$, shows that the null hypothesis cannot be rejected at confidence levels as low as 20 percent (Crow *et al*., Table 3, 1960). Hence, as might be expected the velocities inferred from the fault-normal and fault-parallel data sets cannot be inferred to be from distinct populations. Hence, the apparent rupture velocity implied by the arrivals at surface sites along the fault north of the epicenter ranges between 2.86 ± 0.15 km/sec and 3.03 ± 0.24 km/sec, as implied by the fault parallel and fault normal arrivals, respectively.

A particle motion diagram for the horizontal plane commencing with the onset of the P arrival for a 5 second interval is shown at each location in the array in Figure 7. These horizontal particle motion diagrams, combined with those computed for CGS stations (Shakal *et al*., 2004; p. 37) indicate that the largest horizontal displacements occurred at stations north of the epicenter in a general direction perpendicular to the fault zone. This observation is consistent with that indicated earlier from examination of Figures 3 and 4. The largest observed fault-normal displacements recorded at GEOS stations occurred at the Eades (EFU, 13 cm) and Middle Mountain (MFU, 14 cm) stations. The MFU station is near the terminus of the northern end of the rupture (Langbein *et al*, 2004). The EFU station is about half way between the epicenter and the northern end of the rupture. The particle motion diagrams show that the first motion in the horizontal plane at the sites along the northern section of the fault rupture are in a general northwest direction parallel to the fault for sites west of the fault and in a reversed southeast direction for sites on the east side of the fault. These initial particle motions in the near field are consistent with those for simple right-lateral strike-slip motion as previously indicated in Figures 3 and 6.

The slip distribution inferred for the fault surface using the GEOS recordings and the SMA recording at site CW02 and GPS data by Chen Ji (pers. commun., 2005; Langbein *et al*., 2005) implies a total seismic moment of 9.4×10^{17} Nm and fault rupture for 22 km to the northwest of the epicenter with an average rupture velocity of 2.9 km/sec. The inferred slip distribution for the model with a fault plane dipping at 83° suggests the largest slip northwest of the epicenter occurs at a depth of about 6.5 km beneath the Eades and FZ12 sites. This observation is consistent with the large fault-normal displacements observed in the record sections and particle motions at these sites. The average velocity for the rupture implied by the Ji model is intermediate between the 2.86 km/sec and the 3.03 km/sec implied by the coherent fault-parallel and fault-normal pulses apparent on the displacement record sections.

Liu *et al*. (this volume) using the CGS and GEOS strong-motion recordings at 43 stations inferred a set of 10 models of rupture that they indicate fit the data equally well. Their models indicate that a zone of high slip is located 10 to 25 km northwest of the hypocenter, at a depth between 1 and 10 km, but that the data does not permit the contours of slip in this zone to be resolved precisely. Their models yield a seismic moment of 1.08×10^{18} Nm and indicate that the rupture velocity is highly heterogeneous. They indicate an average rupture velocity along strike northwest of the hypocenter at the depth of the hypocenter of 3.35 km/s. They indicate that rupture velocities for zones closer to the surface northwest of the hypocenter are slower, but did not indicate an average rupture velocity for this zone.

IMPLICATIONS OF HIGH RESOLUTION STRAIN AND ACCELERATION MEASUREMENTS FOR FAULT RUPTURE AND CRUSTAL STRAIN CHANGES

The recordings of volumetric strain at high and low sampling rates (200 sps; 1 sp 10 min.) when considered together with the dense set of acceleration recordings provide a special opportunity to gain insight into the nature of fault rupture and corresponding radiation fields. Volumetric strain meters (Sacks *et al*. 1971; Evertson, 1977) detect volumetric strain variations with periods ranging from 10^{7} seconds to 5×10^{-2} seconds over a dynamic range of

140 dB (Johnston *et al*., 1982; 1984). Empirical observations confirm theoretical predictions that volumetric strain meters detect the divergence of the displacement field. As a result they detect as a scalar, the dilational energy associated with P and Rayleigh-Type surface waves on a layered anelastic Earth, but do not detect rotational energy associated with direct Type-I or Type-II S waves (Borcherdt, 1988; Borcherdt *et al*., 1989). However, when located near a boundary such as the free surface, they detect signals near the time of the S wave arrival due to the conversion of S to P wave energy by the boundary (Borcherdt and Glassmoyer, 1989). High-resolution simultaneous measurements of volumetric strain and acceleration permit the resolution of superimposed dilatational and rotational seismic radiation fields as well as the static and dynamic characteristics of near-source crustal strain changes.

Implications of Co-Located Measurements of Strain and Acceleration for Fault Rupture

The Froelich and Donna Lee sites are of interest for fault rupture considerations, because they are near the fault zone (~ 1.5 km and 3.5 km), but on opposite sides at similar hypocentral distances of 16.8 and 17.2 km. Unprocessed volumetric strain recordings for the Froelich and Donna Lee sites are shown at the same scale in Figure 8. Comparison of the unprocessed traces by superposition of the Donna Lee trace inverted on the Froelich trace (Figure 8) shows that a substantial correlation exists between compression on one side of the fault and dilation on the other side for periods in the 1 to 5 second range.

The volumetric strain signals and velocity signals, filtered with a 3 Hz low-pass filter, are shown in Figure 9 for each of the dilatometer sites. The similarity in the superimposed vertical component velocity and volumetric strain signals at these sites (Figure 9) indicates that the signal registered by the dilatometers for the first 2.2 seconds is that of the initial P wave radiated from the nucleation zone. The superimposed traces in Figure 8 suggest that during the arrival of the P wave the west side of the fault at Froelich is under an average net compression of about 0.6 μstrain for about 2.2 seconds and correspondingly the Donna Lee site is under an average dilation of about -0.5 μstrain .

At about 2.2 seconds after the P arrival the Froelich site undergoes dilation and Donna Lee undergoes compression corresponding to the arrival of S wave energy readily apparent on the fault-parallel and fault-normal components (Figure 9). Inspection of the superimposed velocity and strain traces (Figure 9) shows a phase shift consistent with that expected for conversion of S energy to dilational energy at a non normal angle of incidence by the free surface (Borcherdt and Glassmoyer, 1989). Inspection of the character of the volumetric strain signal at the time of the arrival of the S energy at the Froelich, Donna Lee and the Vineyard Canyon sites (Figure 9) shows that the general character of the first pulse is more similar to that of the fault-parallel velocity than the fault-normal velocity. An explanation for this observation is that the fault-parallel motion interacts with the free surface as SV energy and hence upon reflection generates P wave energy detected by the dilatometer. On the other hand the fault-normal S energy interacts with the free surface more as SH energy, which upon reflection does not generate as much P wave energy and hence is not apparent in the volumetric strain time histories.

The fact that the Froelich and Vineyard Canyon sites on the west side of the fault experience a large pulse in dilation and the Donna Lee site experiences a large pulse in

compression at the time of the arrival of the S energy even though the net coseismic strain offset that occurs at the site is of opposite sign may at first seem contradictory. However, theoretical predictions and numerical estimates of the amplitude and phase reflection coefficients for a Type-I S viscoelastic wave (SV in elastic media) interacting with a free surface (see figures 4c and 4d; Borcherdt and Glassmoyer, 1989; Borcherdt, 1988) indicate that S energy polarized in a plane parallel to the fault plane propagating to the free surface such that the first fault-parallel displacement is in a right lateral sense will give rise to dilational P wave energy at the sites on the west side of the fault and to compression energy on the east side, consistent with that observed.

Implications of High-Resolution Strain Measurements for Dynamic and Static Crustal Strain Changes

Comparison of the high-resolution (200 sps) measurements of volumetric strain obtained during the time interval that seismic energy is radiated by fault rupture with those obtained at a lower sample rate (1 sample per 10 minutes) over long time intervals provides a special opportunity to answer questions concerning how quickly strain offsets occur and how they vary with time.

The low and high sample rate recordings of volumetric strain are plotted for each site (Figure 10). The first trace shown for each site is that recorded via GOES satellite for a three day period at a sampling rate of 1 sample per 10 minutes (Johnston *et al*, this volume). The second trace is that recorded for 80 seconds via GEOS at 200 sps. The third trace is the 200 sps recording filtered with a 10 second, high-cut, 2 pole Butterworth filter.

The low sample rate recordings show well-defined strain offsets superimposed on corresponding Earth tidal signals. Strain offsets as measured directly from the low-sample rate data at the first 10 minute sample which occurred about 5 minutes after the earthquake and at 24 hours are summarized in Table 1 (columns 3, 4). (see Johnston *et al*., this volume for detailed discussion of offsets measured from low-sample rate recordings).

The high-sampling rate (200 sps) recordings of volumetric strain at each site, (trace 2, Figure 10) show that the dynamic strain changes that occur during the time of the strongest seismic radiation are more than an order of magnitude larger than the coseismic offsets. The coseismic offsets are apparent as a small shift in baseline (trace 2 for each recording location, Figure 10). Hence, to better resolve the coseismic offset as observed at high sampling rates, it is necessary to filter the signals to remove the dominant dynamic signals that occur at higher frequencies.

The high-cut filtered traces, (trace 3 for each recording location, Figure 10) reveal a well-defined coseismic offset for each site. The traces show that a stable estimate of the offset can be measured over a time interval of about 20 seconds initiating with the arrival of the P wave. The filtered traces show that a net strain offset begins at the time of the P wave arrival at each site, but that the predominant strain offset at each of the sites begins at the time of the arrival of the large horizontal fault-normal and fault-parallel pulses at each site (compare Figures 8 and 10). The high-resolution traces show that the dominant coseismic strain offset occurs over a time interval of about 10 seconds at each of the three sites nearest the fault and over an

interval of about 15 seconds for the more distant Red Hills site. The occurrence of the dominant coseismic strain offset at the time of the dominant fault-normal and fault-parallel pulses suggests that the dominant pulse and the corresponding coseismic strain offsets at the Froelich, Vineyard Canyon, and Donna Lee sites are evidence of the dislocation or fault slip propagating northwestward beneath and past these sites along the fault. The amplitude of the high-resolution, coseismic strain offset apparent in the filtered traces at about 20 seconds after the P arrival together are tabulated (Table 1, column 2). For completeness the strain offsets as measured directly from the time histories in columns 2, 3, and 4 are also shown in columns 8, 9, and 10 after normalization by a tidal response factor derived to account for variations in the local response of each of the sites to tidal loading (Johnston *et al*., 1982; this volume).

The high-resolution coseismic strain offsets at 20 seconds indicate compression at the Froelich and Vineyard Canyon sites on the west side of the fault and dilation at the Donna Lee site on the east side of the fault. These coseismic strain offsets are consistent with what is predicted by Hisada's model for volumetric strain resulting from right-lateral movement on a strike-slip fault (Hisada, 2005, personal commun.).

Comparison of the high-resolution strain offsets inferred at 20 seconds with those inferred from the low-sampling rate recordings after the earthquake permits accurate inferences of post event strain changes with time. Post-event strain changes inferred as the difference between the coseismic strain offset at 20 seconds and those at 5 minutes and 24 hours after the initial P arrival are tabulated (Table 1, columns 5 and 6). Comparison of these post event strain offsets with the coseismic offset at 20 seconds shows that the post event strain changes continue to increase significantly with time. Over a 24 hour period the strain offsets at Froelich, Vineyard Canyon, Donna Lee, and Red Hills increase in the same sense as the initial strain offset by 301, 30, 71, and 110 percent, respectively. The largest observed post-event strain change at 24 hours occurs at the Froelich site, which is the site closest to the northern end of the southwest fracture zone. The post-event change at this site is about 200 percent of the coseismic strain offset. The inferred post-event changes suggest that considerable redistribution of regional strain continues after the initial abrupt offset that occurs with fault rupture at the depth of the hypocenter (see Johnston *et al*. this volume for additional discussion).

The strong dependence of strain offsets on time after the initial rupture, as shown by these high-sample rate measurements, suggests that the magnitude of strain offsets need to be presented in the future in the context of the sampling resolution and the time interval over which the offset is measured. For example, strain offsets inferred here from the high-sampling rate recordings would be referred to as *"coseismic strain offsets inferred over a time interval of 20 seconds after the P wave arrival from 200 sps recordings"*. These results suggest that offsets measured at sampling intervals longer than the duration of shaking over longer intervals of time should be similarly identified with the term "coseismic" reserved for offsets measured at high sampling rates.

Implications for Dynamic Fault Straining and Triggered Fault Rupture

The dynamic and static-offset strain measurements at sites along and on both sides of the fault provide a basis to estimate strains in the fault zone and discuss their possible role in facilitating fault rupture. The time histories in Figure 8 show that the Froelich site experiences

maximum compressions of 1.7 μstrain during the initial P wave, maximum dilation and compression of -4.9 and +5.9 μstrain, respectively during the passage of fault rupture, and a maximum static coseismic strain offset of 0.206 μstrain within 10 seconds of the arrival of the S wave. Similarly, the Donna Lee site experiences maximum dilation of -1.1 μstrain during the initial P wave, maximum compression and dilation of 4.2 and -3.5 μstrain, respectively, during passage of fault rupture, and a maximum static coseismic strain offset of -0.157 μstrain within 10 seconds of the arrival of the S wave.

During the arrival of the P wave energy, the measurements suggest that the fault zone is experiencing a combined maximum compression on the west side and maximum dilation on the east side that is 7.7 times greater than the final combined coseismic offset at the sites. Assuming that the initial P wave energy is due mostly to radiation associated with nucleation and rupture in the immediate hypocentral region, the measurements indicate that radiation from the initial rupture zone is generating maximum dynamic strain variations near the fault zone (1.7 μstrain) that are significantly greater than the final static offsets (0.206 μstrain) associated with coseismic fault slip.

During the arrival of the S wave energy, the measurements show that the fault zone is experiencing maximum compression on the west side and maximum dilation on the east side that are at least 29 and 22 times greater than the final coseismic offset. Assuming that the maximum strains during the arrival of the S wave energy are due in large part to passage of the rupture and considering that the Froelich and Donna Lee sites are about 2.0 km and 3.5 km, respectively from the fault zone, suggests that the maximum strains at the edge of the fault zone are larger than those observed away from the zone. Hence, the recordings suggest that the fault zone is experiencing maximum dynamic volumetric strains on opposite sides of the fault zone that are more than an order of magnitude greater than the coseismic strain offset due to slip on the fault.

These measured differences in the amplitude of the dynamic strain on the two sides of the fault and observed static offsets suggest that strain loading and unloading of the fault due to energy radiated from parts of the fault that are rupturing is significantly greater than the final strain release on the fault as influenced by the regional static strain field. These relatively large high resolution measurements of strain variations across the fault provide empirical evidence that dynamic strain variations radiated from the initial nucleation zone and subsequent rupturing could contribute to the triggering of additional rupture and extension in rupture on the fault surface (Gomberg, 2001).

IMPLICATIONS OF CO-LOCATED MEASUREMENTS

Co-located measurements of volumetric strain and velocity for incident P and S waves have been shown to permit inferences of wave-field characteristics and local constitutive properties not permitted by either measurement alone (Borcherdt, 1988; Borcherdt *et al*., 1989). An expression showing this result will be specified here. The expression is used to infer single station estimates of local material velocities as well as compare strain-meter response characteristics inferred at tidal periods with those for accelerometers inferred at seismic frequencies.

The free-surface vertical reflection coefficient for a P wave incident on the surface of a viscoelastic solid is defined as the ratio of the maximum vertical displacement at the free surface due to the incident and reflected waves to the maximum vertical amplitude of the incident P wave. The expression for the vertical reflection coefficient for a general (homogeneous or inhomogeneous) P wave incident on the free surface of a viscoelastic solid is

$$r_{zP} = \frac{Max.Vert.\,Free\ Surface\ Disp.}{Max.Vert.\,Disp.\,of\ \ Inc.\,P} = \left(\frac{Max.Vert.\,Free\ Surface\,Velocity}{Max.Vol.\,Strain\,of\ \ Inc.\,P} \right) \frac{1}{v_{HP}} \sqrt{\frac{2\chi_{HP}}{1+\chi_{HP}}} \frac{1}{\left|\vec{\xi}_1\right|} \tag{1}$$

where

v_{HP} represents the local P velocity for a homogenous wave in the material,

$\chi_{HP} \equiv \sqrt{1+Q_{HP}^{-2}}$ is defined in terms of the reciprocal quality factor Q_{HP}^{-1} for a homogenous P wave,

and $\left|\vec{\xi}_1\right|$ represents the length of the major axis of the particle motion ellipse for the incident P wave (Borcherdt, 1988).

For incident homogenous P waves and materials with $Q_{HP} \geq 30$, $\chi_{HP} \approx 1$, hence the expression for the reflection coefficient for the vertical component of motion reduces to

$$r_{zP} \approx \frac{1}{v_{HP}} \left(\frac{Max.Vert.\,Free\ Surface\,Velocity}{Max.Vol.\,Strain\,of\ \ Inc.\,P} \right) = \frac{1}{v_{HP}} \left(\frac{\dot{u}_{z_{\max}}}{\frac{\Delta V}{V}_{\max}} \right) . \tag{2}$$

This expression shows that measurements of the maximum amplitude of volumetric strain for an incident P wave and the corresponding maximum velocity at the free surface due to the incident P and reflected waves together with an estimate of the local homogenous P wave velocity provides an estimate of the vertical reflection coefficient. Alternatively, estimates of the angle of incidence for the incident P wave can be used together with model estimates of the reflection coefficient to constrain estimates of the local material velocity of a homogeneous P wave.

A calculated value of the free-surface reflection coefficient assuming an average angle of incidence at the sites of about 15 degrees is 1.88 (Borcherdt and Glassmoyer, 1989). The measured maximum values of vertical velocity at the free surface must necessarily include the effect of the average change in velocity gradient between the dilatometer at depth and the free surface. Hence, if the average velocity at the depth of the dilatometer is specified and the reflection coefficient is approximately known, then expression (2) can be used to also estimate an average amplification factor, F_1, at each site.

Maximum amplitudes of the first P wave pulse (measured peak to trough, see Figure 9) as observed on the volumetric strain recordings and the vertical component of velocity are tabulated in Table 2. Measured values of P velocities at the depths of the dilatometers also are

tabulated in Table 2. The measured values of P velocity for the Vineyard Canyon and Red Hills sites are those derived by Boore (2003) from the borehole velocity logs compiled by Gibbs *et al*. (1990). Measurements of P velocity also exist for the Stockdale (3.1 km/s; 155 m) and the Jack Canyon (2.65 km/s; 95m) sites. The measured values shown for the Froelich and Donna Lee sites represent an average of the velocities inferred at the bottom of the boreholes for the four sites.

Estimates of local P velocities derived from the simultaneous measurements of vertical velocity and volumetric strain, an assumed average amplification factor of 2, and equation (2) also are tabulated in Table 2. Comparison of these estimated P wave values with corresponding measured values for Vineyard Canyon and Red Hills shows that they are in good agreement. Conversely, substitution of the measured values of P velocities into equation (2), permits an estimate of the amplification factor F_1 to be readily derived as tabulated (Table 2). The tabulated values of F_1 are in reasonable agreement with those expected.

Considering that the dilatometers are permanently installed and calibration techniques applied during installation are no longer possible, evaluation of the response characteristics of the dilatometers using the co-located measurements from the accelerometers provides an important opportunity to evaluate the current response characteristics of the dilatometers. The general consistency in the measured and estimated P values suggest that calibration factors developed for the installed volumetric strain meters have remained relatively constant over the last two decades. They indicate that consistency in the response of the dilatometers as observed at tidal periods extends to the observed seismic bandwidth as well (20 seconds - 20 Hz). Establishment of consistency in their response provides support for measurements and conclusions derived to date.

CONCLUSIONS

The 2004 Parkfield earthquake generated a unique set of high-resolution measurements of acceleration, volumetric strain, and velocity on the near-field Borehole-Strainmeter Array (Johnston, et. al,1982), the GEOS Strong-Motion Array, (Borcherdt *et al*., 2004), and the CGS Strong-Motion Arrays (Shakal, et. al, 2004). These arrays, designed to specifically record the near field motions and strains for a M6.0 earthquake along the section of the fault that ruptured, have provided an unprecedented set of high resolution measurements to investigate a number of scientific and engineering issues that could not be investigated previously.

The GEOS high sampling-rate recordings indicate that no precursory strain or displacement signal was discernable for 25 seconds prior to nucleation at detection levels as low as 0.01 nanostrain and 0.5 nanometers at three stations within 17 to 21 km of the hypocenter and 1.5 to 3.5 km of the fault zone. Similarly, pre-event recordings for 2.3 seconds at six other stations at distances between 8.5 to 25 km of the hypocenter and 0.5 to 8 km of the fault zone showed no apparent precursory signal. The lack of a precursory signal at these sensitivities suggests that if precursory signals are to be identified then instrumentation will need to be placed closer to the nucleation zone for M6 events.

The strong-motion recordings obtained on the near-field arrays provide an unprecedented description of fault rupture and its subsequent radiated field as evident in vertical, fault-parallel, and fault-normal displacements inferred at sites located at regular intervals along both sides of the fault. The recordings reveal coherent pulses of fault-parallel and fault-normal displacement indicative of right-lateral displacement on the fault. They show that fault-normal displacements are significantly larger than the fault-parallel and vertical displacements with implications for site-specific, earthquake-resistant design of some structures. The fault-parallel and fault-normal displacement pulses generated by rupture at depth imply apparent rupture velocities along the surface of 2.86 ± 0.15 and 3.03 ± 0.24 km/sec, respectively. Characteristics of the pulses are consistent with model predictions of "fling" and "directivity" associated with rupture to the northwest on a strike-slip fault (Hisada and Bielak, 2003).

The 200 sps recordings of volumetric strain at sites on opposite sides of the fault provide unprecedented measurements of dynamic and coseismic strain offsets across the fault zone. High-cut filtered versions of the recordings show that the true coseismic strain offsets occur over time intervals of less than 10 seconds. Comparison of the recordings with those of three-component velocity inferred from co-located accelerometers shows the coseismic offset occurs at the time of arrival of the dominant fault-parallel and fault-normal displacements associated with fault rupture. The co-located recordings indicate that the abrupt coseismic offset over a 10 second interval is associated with coseismic slip on the fault.

The high-sampling rate recordings indicate that the maximum dynamic compressions and dilations being experienced on opposite sides of the fault are in the same sense, but more than an order of magnitude larger than the abrupt coseismic static offsets associated with coseismic fault slip. The recordings show that dynamic straining of the fault zone due to radiation from other rupturing segments of the fault is significantly larger than the strain release associated with fault slip. Hence, the recordings provide empirical measurements to suggest that dynamic strains on the fault due to seismic radiation may trigger and extend rupture onto previously unruptured nearby segments of the fault.

The high resolution coseismic strain offsets inferred at 20 seconds after the initial P arrival are consistent with static model estimates for right-lateral, strike-slip fault movement. These estimates when compared with those inferred at 5 minutes and 24 hours after the earthquake show that the strain release across the fault zone continues to increase by as much as 69 percent in 5 minutes and 300 percent in 24 hours for the site closest to the northern end of the southwest fracture zone (Froelich). These measurements show that in the case of the Parkfield earthquake the high-resolution measurement of the co-seismic strain offset which occurs over a 10 second interval is only a fraction of the post-event offset which occurs more gradually over time periods of minutes, hours, and days. They indicate that the abrupt offset measured at high resolution over an interval of 10 seconds is due to coseismic fault slip. The post event measurements of offset at 5 minutes and 24 hours indicate that the regional strain field continues to change in the same sense as that associated with the initial coseismic slip on the fault. They indicate that the gradual post-event changes in strain as observed at the surface over long time intervals after the earthquake can be several times larger than those that occur abruptly with slip at depth at the time of the earthquake.

Co-located measurements of volumetric strain and acceleration of the Parkfield M6 earthquake provide an important opportunity to compare the consistency in response of the dilatometers as determined at tidal periods with that observed at seismic periods. Comparison

of measured and estimated values of local P wave velocity and amplification factors show relatively good agreement at sites for which measurements exist. This agreement helps confirm that the response characteristics of the dilatometers have remained constant with time at seismic periods as well as at tidal periods.

ACKNOWLEDGEMENTS

We appreciate the cooperative efforts of Anthony Shakal and the California Geological Survey Strong-Motion Instrumentation Program and the excellent CGS strong-motion data set. We would like to extend a special acknowledgment to Doug Myren for his efforts in maintaining the dilatometer transmission electronics. Review comments by Ruth Harris, Guo-Quan Wang, Anthony Shakal, William Bakun, Matthew Dalleso, and an anonymous reviewer are appreciated. Dave Boore's v_S data base was helpful in finding the velocity measurements of Gibbs *et al*. (1990) at the borehole sites.

REFERENCES

Bakun, W. H., and A. G. Lindh (1985). The Parkfield, California earthquake prediction experiment, *Science*, **229,** 619-624.

Boore, D. M. (2003). A compendium of P- and S- velocities from surface-to-borehole

logging: summary and reanalysis of previously published data and analysis of unpublished

Data, *U. S. Geol. Survey OF Rept. 2003-191,* 14 pp.

Borcherdt, R. D., J. B. Fletcher, E. G. Jensen, G. L. Maxwell, J. R. Van Schaack, R. E. Warrick, E. Cranswick, M.J.S. Johnston, and R. McClearn, R. (1985). A general earthquake observation system (GEOS), *Bull. Seismol. Soc. Am.,* **75,** 1783-1825.

Borcherdt, R. D., and M. J. S. Johnston (1988). A broadband, wide dynamic range, strong-motion net-work near Parkfield, California, USA for measurement of acceleration and volumetric strain, Ninth World Conference on Earthquake Engineering, Proceedings, **VIII,** 125-130.

Borcherdt, R. D. (1988). Volumetric strain and particle displacements for body and surface waves in a general viscoelastic half-space, *Geophysical Journal of the Royal Astronomical Society*, **93,** 215-228.

Borcherdt, R. D. (1988). Recording strong motion - new methods and instrumentation in the U.S., *Jour. Int'l. Council Bldg. Res. (CIB),* **16,** 87-92.

Borcherdt, R. D., M. J. S. Johnston, and G. Glassmoyer (1989). On the use of volumetric strain meters to infer additional characteristics of short-period seismic radiation, *Bull. Seismol. Soc. Am.,* **79,** 1006-1023.

Borcherdt, R. D., and G. Glassmoyer (1989). An exact anelastic model for the free-surface reflection of P and S-I waves, *Bull. Seismol. Soc. Am.,* **79,** 842-859.

Borcherdt, R. D., M. J. S. Johnston, C. Dietel, G. Glassmoyer, D. Myren, and C. Stephens (2004). Acceleration and volumetric strain generated by the Parkfield 2004 Earthquake on the GEOS Strong-Motion Array near Parkfield, CA, *U. S. Geol. Survey OF Rept.2004-1376*, 74 pp.

Evertson, D. W. (1977). Borehole strain meters for seismology, Rep. ARL-TR-77-62, Applied Research.

Gibbs, J. F., E. F. Roth, T. E. Fumal, N. A. Jasek, and M. A. Emslie (1990). Seismic velocities from borehole measurements at four locations along a fifty-kilometer section of the San Andreas fault near Parkfield, CA, *U. S. Geol. Survey OF Rept. 1990-248*, 34 pp.

Gomberg, J. (2001). The failure of earthquake failure models, Journal Geophysical Research, 106, 16253-16263.

Hisada, Y. and J. Bielak (2003). A theoretical method for computing near-fault ground motions in layered half-spaces considering static offset due to surface faulting, with a physical interpretation of fling step and rupture directivity, *Bull. Seismol. Soc. Am.,* 93, 1154-1168.

Johnston, M. J. S., A. T. Linde, I. Sacks, and D. Myren (1982). Borehole dilatometer strain array -- Installation and preliminary results from the Mojave desert, *EOS,* **63,** 430.

Johnston, M. J. S. and R. D. Borcherdt (1984). Earth strain in the period range 0.1-10,000 seconds at six borehole sites within the San Andreas fault system, *EOS,* **65,** 1015.

Johnston, M. J. S., R. D. Borcherdt, and A. T. Linde (1986). Short-period strain (0.1-105 s): near-source strain field for an earthquake (ML 3.2) near San Juan Bautista, California, *J. Geophys. Res.,* **91,** 11,497-11,502.

Johnston, M. J. S., A. T. Linde, M. T. Gladwin, and R. D. Borcherdt (1987a). Fault failure with moderate earthquakes, *Tectonophysics,* **144,** 189-206.

Johnston, M. J. S., R. D. Borcherdt, M. T. Gladwin, G. Glassmoyer, and A. T. Linde (1987b). Static and dynamic strain during the ML 5.9 Banning, California, earthquake on July 8, 1986, *EOS,* **68,** 1244.

Johnston, M. J. S. and A. T. Linde (2002). Implications of crustal strain during conventional, slow, and silent earthquakes, *International handbook of Earthquake and Engineering Seismology*, **81A**, 589-605.

Johnston, M. J. S., R. D. Borcherdt, A. T. Linde, and M. T. Gladwin (2006). Continuous borehole strain and pore pressure in the near-field of the September 28, 2004, M_W 6.0 Parkfield, California earthquake: Implications for nucleation, fault response, earthquake prediction, and tremor, *Bull. Seismol. Soc. Am.,* this volume**,** ?-?.

Langbein, J., R. Borcherdt, D. Dreger, J. Fletcher, J. Hardebeck, M. Hellweg, C. Ji, M. Johnston, J. Murray, R. Nadeau, M. Rymer, and J. Treiman (2004). Preliminary report on the 28 September 2004, M 6.0 Parkfield, California earthquake, *Seismol. Res. Letters,* **76,** 10-26.

Liu, P., S. Cust´odio, R. J. Archuleta (2006), Kinematic inversion of the 2004 M_W 6.0 Parkfield earthquake including site effects, *Bull. Seismol. Soc. Am.*, ?-?

Mueller, R. J., M. Lee, M. J. S. Johnston, R. D. Borcherdt, G. Glassmoyer, and S. Silverman (1995). Near-real time monitoring of seismic events and status of portable digital recorders using satellite telemetry, *Bull. Seismol. Soc. Am.,* **85,** 640-645.

Rymer, M. J., J. C. Tinsley, J. A. Treiman, J. R. Arrowsmith, K. B. Clahan, A. M. Rosinski, W. A. Bryant, H. A. Snyder, G. S. Fuis, N. Toké, and G. W. Bawden (2006). Surface fault slip associated with the 2004 Parkfield, California, earthquake, *Bull. Seismol. Soc. Am.*, this volume ?-?

Sacks, I. S., S. Suyehiro, D. W. Evertson, and Y. Yamgishi (1971). Sacks-Evertson strain meter, its installation in Japan and some preliminary results concerning strain steps, *Papers Meterol. Geophys.* **22,** 195-207.

Shakal, A., M., V. Graizer. M. Huang, R. Borcherdt, H. Haddadi, K. Lin, C. Stephens, and P. Roffers (2005). Preliminary analysis of strong-motion recordings from the 28 September 2004 Parkfield, California earthquake, *Seismol. Res. Letters,* **76,** 27-39.

Somerville, P. G., H. Krawinkler, and B. Alavi (2000). Development of improved ground motion representation and design procedures for near-fault ground motions, Final Rept. to CSMIP Data Utilization Program, Calif. Geol. Survey, Sacramento, CA.

Spudich, P., L. Baker, and J. Fletcher (1988). The USGS dense seismic array at Parkfield, California: Instrumentation and data analysis, in Yeh, Y. T., and H. C. Chiu, eds., International Workshop on Strong Motion Arrays, 2nd, Taipai, Taiwan, 16-19 Jan. 1988, Proceedings: Taipai, Taiwan, Institute of Earth Sciences, Academic Sinica, 123-134.

FIGURE CAPTIONS

Figure 1. Map showing location of stations in GEOS Parkfield array, sensor types at each station, (accelerometer, A; velocity transducer, V; and dilatometer, D) and 15 seconds of acceleration and volumetric stain recorded at each site.

Figure 2. Pre-event displacement (a, b) and volumetric strain (c) time histories and maximum amplitudes recorded immediately prior to the occurrence of the arrival of the first P wave energy. The pre-event 200 sps recordings indicate no precursory signals. If precursor signals exist, the recordings show that their amplitude would be less than the maximum displacement amplitude of 0.5 nanometers and the maximum strain amplitude of 0. 15 nanostrain.

Figure 3. Fault-parallel displacement inferred from CGS(SMA-1) and USGS (GEOS) acceleration recordings of the Parkfield 2004 earthquake at sites along the fault north of the epicenter arranged with time increasing to the left for sites on the west side of the fault and to the right for sites on the east side of the fault.

Figure 4. Fault-normal displacement inferred from CGS(SMA-1) and USGS (GEOS) acceleration recordings of the Parkfield 2004 earthquake at sites along the fault north of the epicenter arranged with time increasing to the left for sites on the west side of the fault and to the right for sites on the east side of the fault.

Figure 5. Vertical displacement inferred from CGS(SMA-1) and USGS (GEOS) acceleration recordings of the Parkfield 2004 earthquake at sites along the fault north of the epicenter arranged with time increasing to the left for sites on the west side of the fault and to the right for sites on the east side of the fault.

Figure 6. Travel times and inferred average rupture velocities for the initial fault-parallel (a) and fault-normal (b) displacement pulses together with corresponding regression curves, 95% confidence limits for the observed values, and the 95% confidence limits for the ordinate to the true population regression line.

Figure 7. Horizontal particle motions inferred from displacement time histories recorded on the GEOS array.

Figure 8. **V**olumetric strain time histories as recorded at the Froelich and Donna Lee sites, also shown with the Donna Lee recording inverted and superimposed on that from Froelich. The superimposed recordings show that a strong correlation exists between compression and dilation at

frequencies as high as 1 Hz at these two sites at distances of about 2 and 3.5 km on opposite sides of the fault.

Figure 9. Borehole volumetric-strain time histories superimposed on inferred three-component, co-located, surface velocity time histories as filtered with a 3Hz, 2 pole Butterworth, high-cut filter indicate that the strain meters detect direct P waves and P waves generated at the free surface by incident S waves with a component of particle motion perpendicular to the surface.

Figure 10. Original volumetric strain recordings of the Parkfield 2004 earthquake shown at a low-sample rate (1 sample per 10 minutes) for a three-day time interval and at a high-sample rate (200 sps) for an 80 second time interval, and a version of the 200 sps time histories filtered with a 10 second 2 pole Butterworth high-cut filter. The time histories indicate at sites near the fault abrupt coseismic strain offsets occur over 10 second time intervals at the time of the arrival of dominant fault-parallel and fault-normal motion. Post event measurements of these strain offsets at later times (e.g. 24 hours) show that strain changes not necessarily associated with coseismic fault slip continue to increase with time.

Table 1. Volumetric strain offsets and post event strain changes for Parkfield 2004 event.

Station	Volumetric Strain Changes (microstrain)								
	Measured Strain Offsets			Post-Event Strain Changes		Norm.	Norm. Strain Offsets		
	20 sec	~ 5 min	24 hrs	~ 5 min*	24 hrs*	Factor	20 sec	~ 5 min*	24 hrs*
Froelich	0.206	0.359	0.794	0.153	0.588	1.7	0.350	0.610	1.350
Donna Lee	-0.157	-0.231	-0.292	-0.074	-0.135	3.63	-0.570	-0.840	-1.060
Vineyard Cyn	0.538	0.612	0.551	0.074	0.013	7.8	4.200	4.776	4.300
Red Hills	-0.011	-0.096	-0.016	-0.085	-0.005	6.04	-0.064	-0.580	-0.095

*Johnston, 2004

Table 2. Local material parameters as inferred from simultaneous measurements of vertical particle velocity and volumetric strain.

Station	$\dot{u}_{z_{max}}$ cm/s	$\frac{\Delta V}{V}_{max}$	r_{zP} calc.	v_{HP} Meas. km/sec	Dil. Depth m	v_{HP} Est. km/sec	F_1	
Froelich	0.464	0.49	1.88	2.97*	223	2.5	1.68	1.70
Donna Lee	-0.683	-0.43	1.88	2.97*	176	4.2	2.83	3.63
Vineyard Cyn	0.554	0.38	1.88	3.98	200	3.9	1.96	7.80
Red Hills	-0.842	-0.94	1.88	2.18	180	2.4	2.18	6.04

*Average

Figure 1. Borcherdt et al., MS # 2005827, BSSA Parkfield 2004 Special Issue

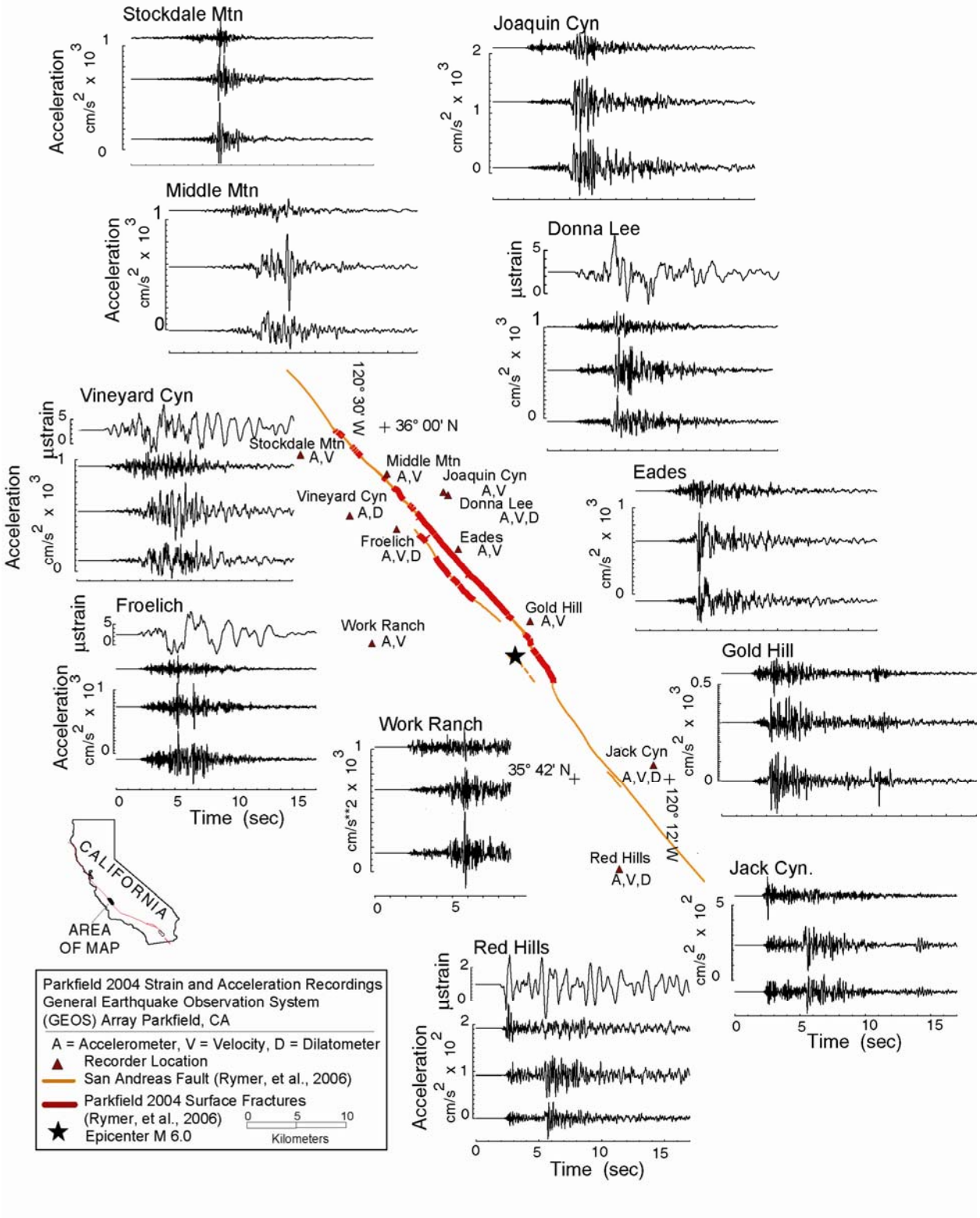

Figure 2. Borcherdt et al., MS # 2005827
BSSA Parkfield 2004 Special Issue

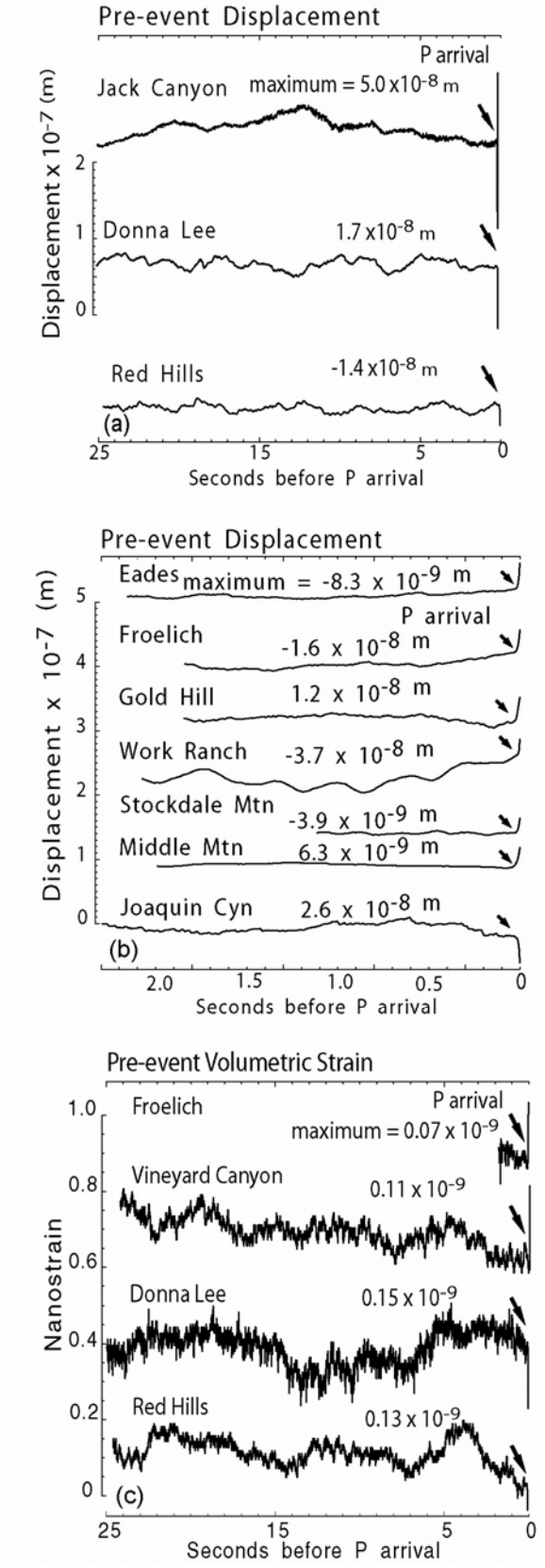

Figure 3. Borcherdt et al., MS # 2005827 BSSA Parkfield 2004 Special Issue

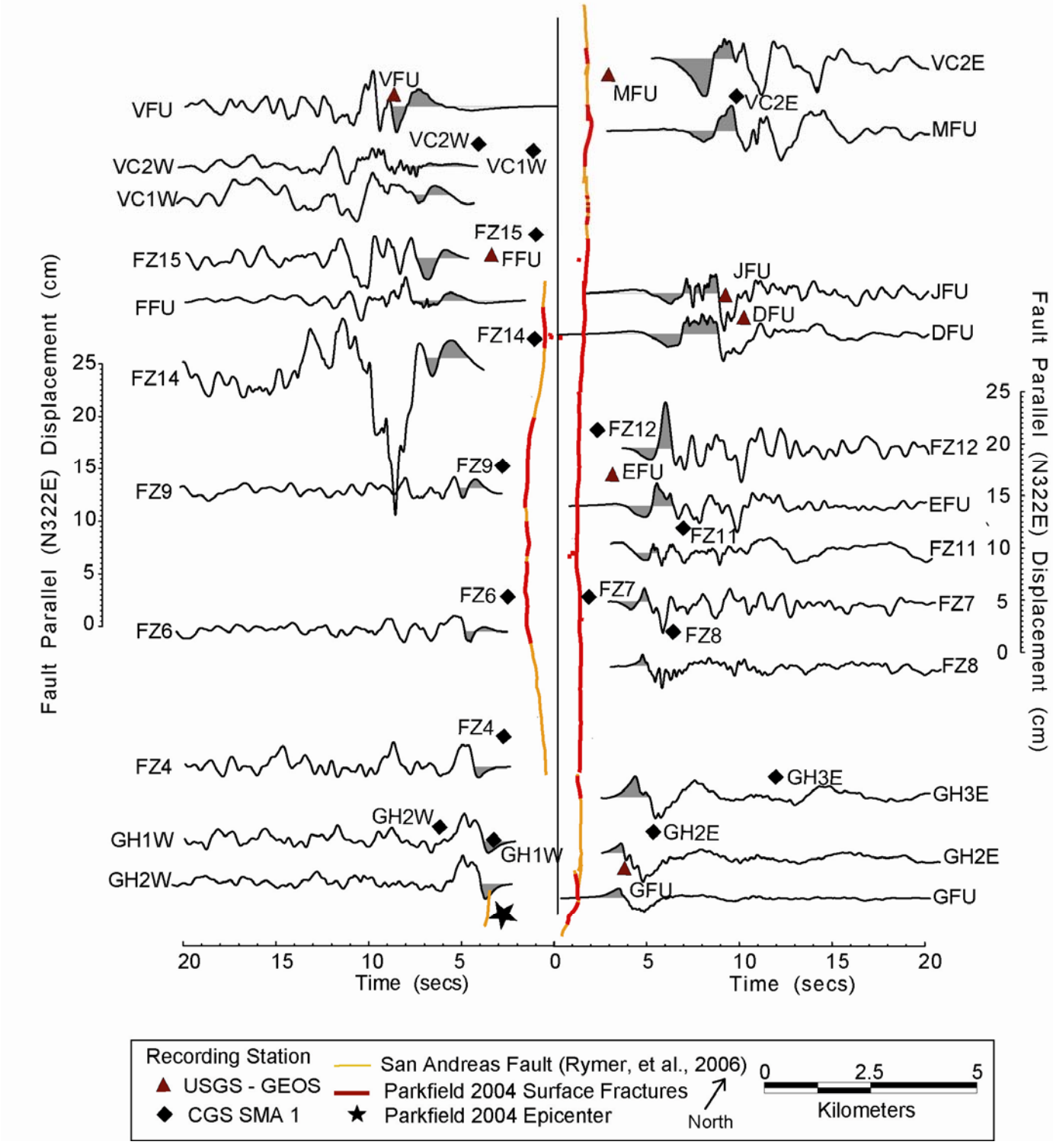

Figure 4. Borcherdt et al., MS # 2005827 BSSA Parkfield 2004 Special Issue

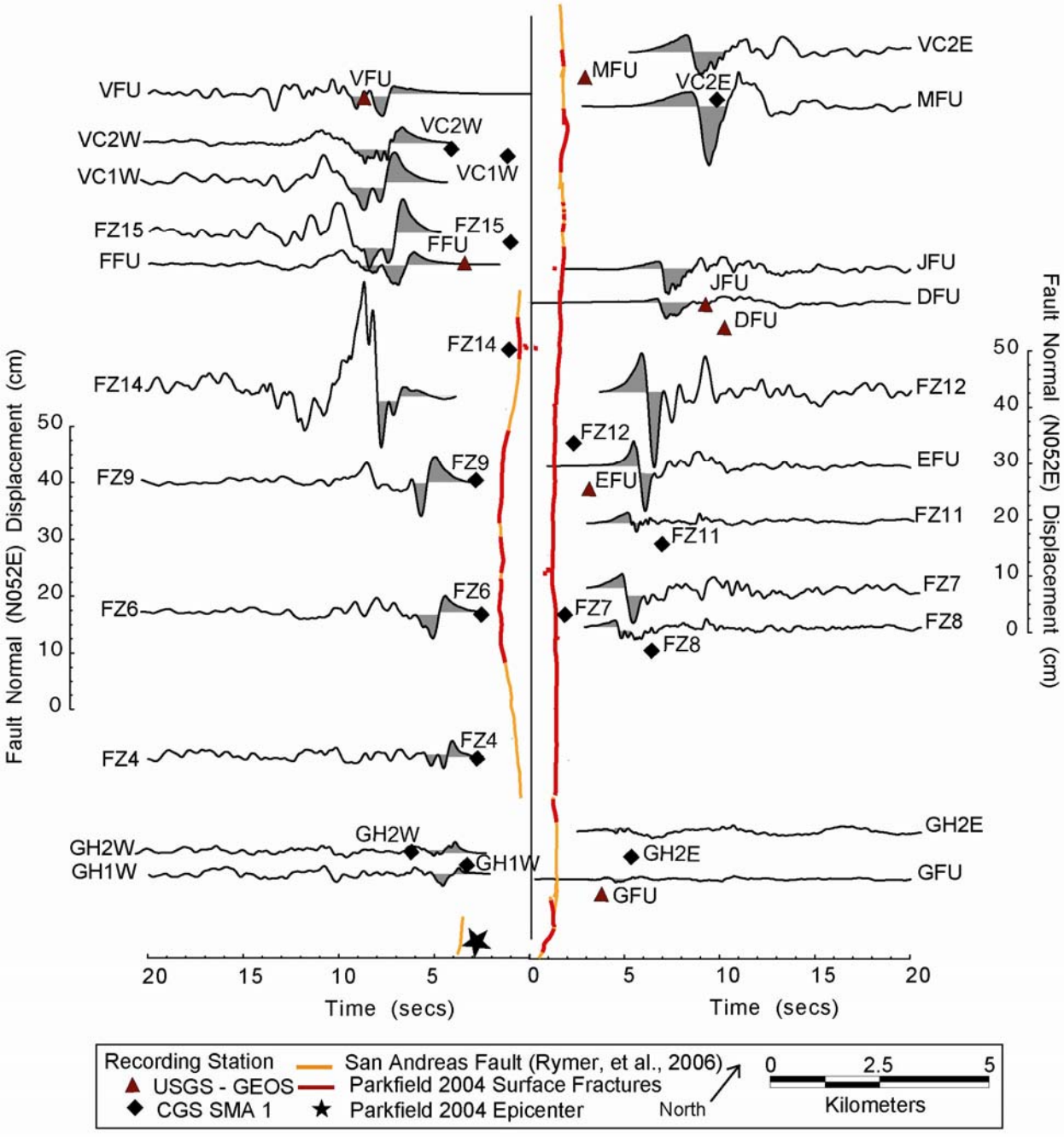

Figure 5. Borcherdt et al., MS # 2005827 BSSA Parkfield 2004 Special Issue

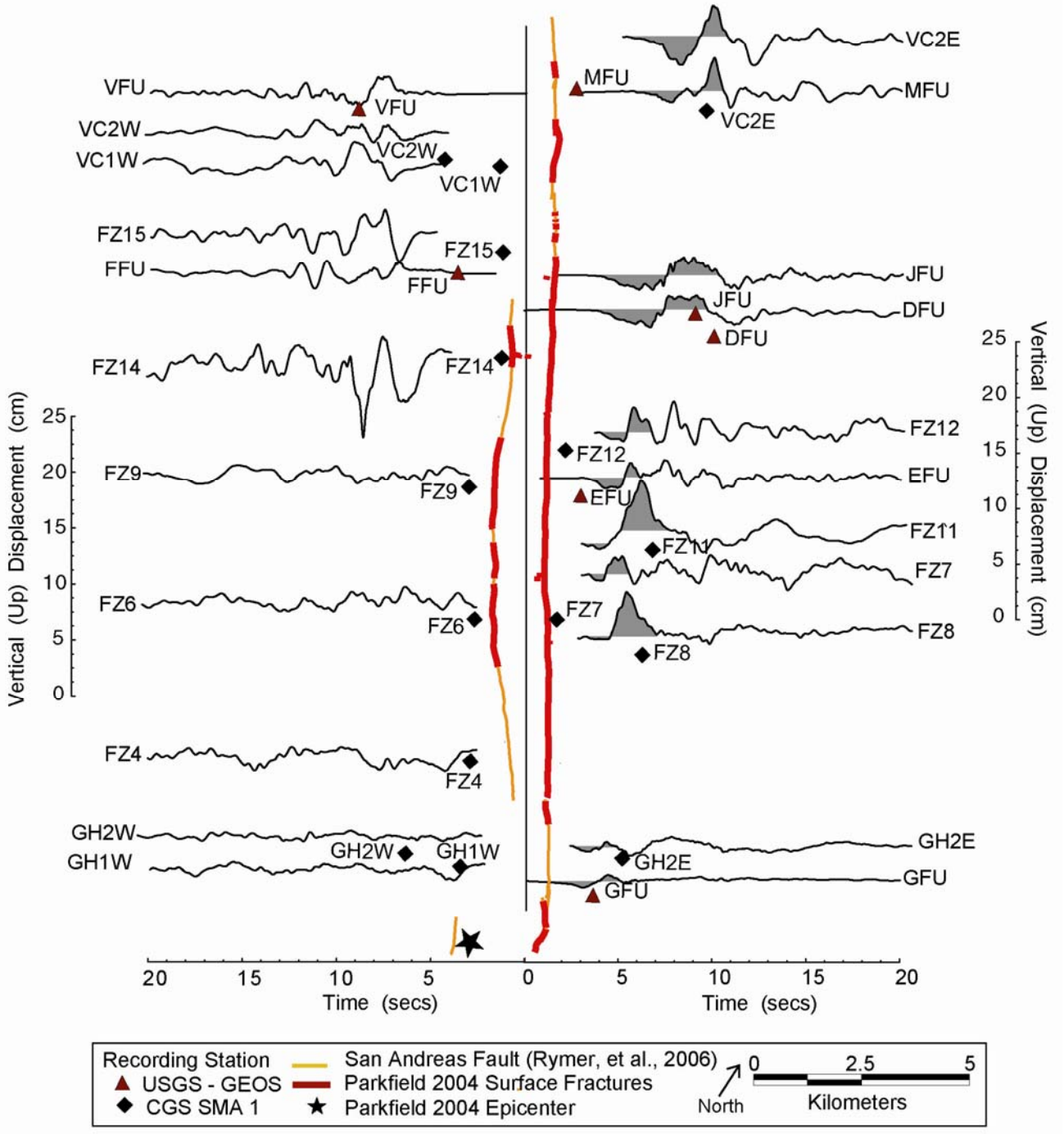

Figure 6. Borcherdt et al., MS # 2005827 BSSA Parkfield 2004 Special Issue

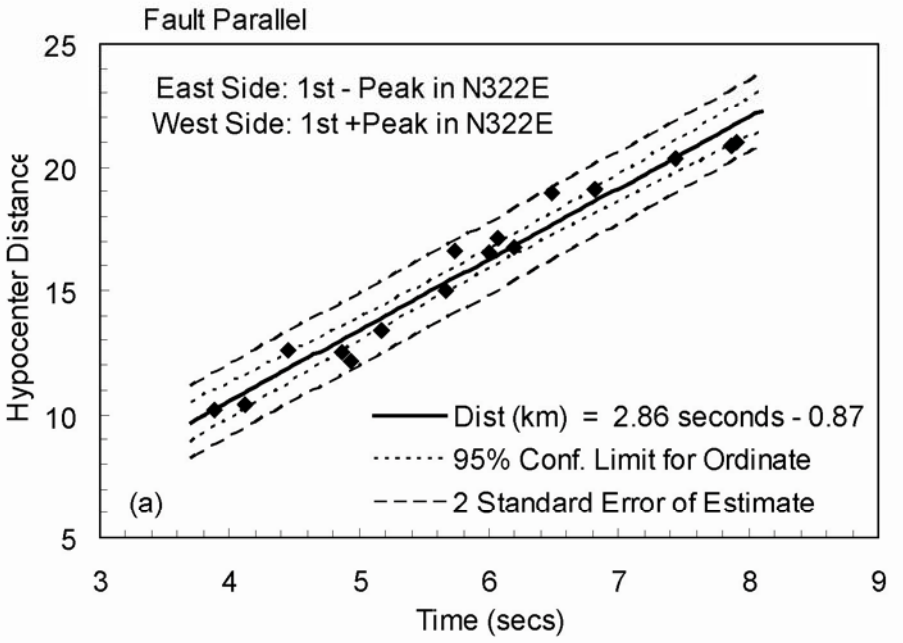

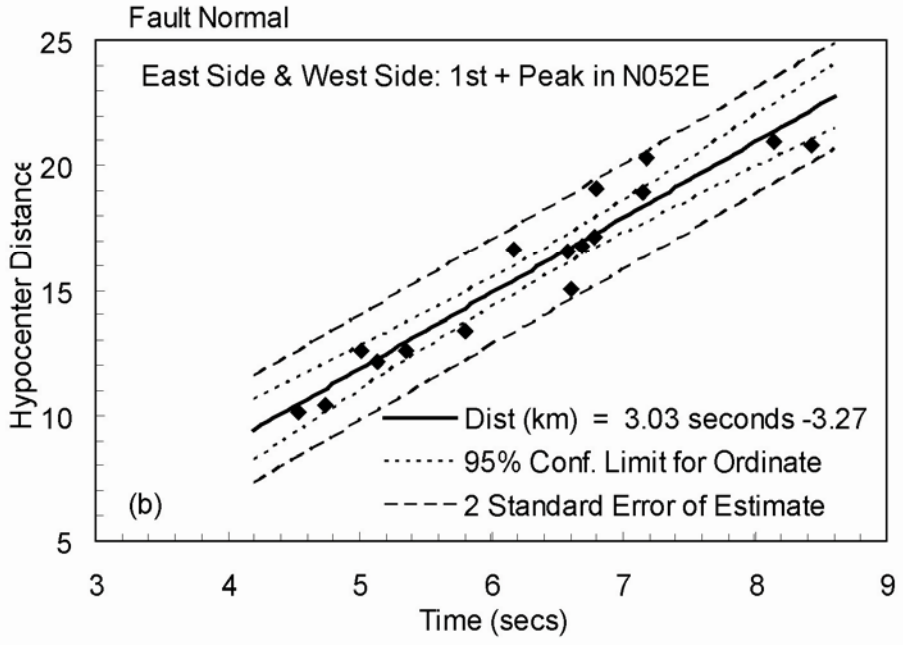

Figure 7. Borcherdt et al., MS # 2005827 BSSA Parkfield 2004 Special Issue

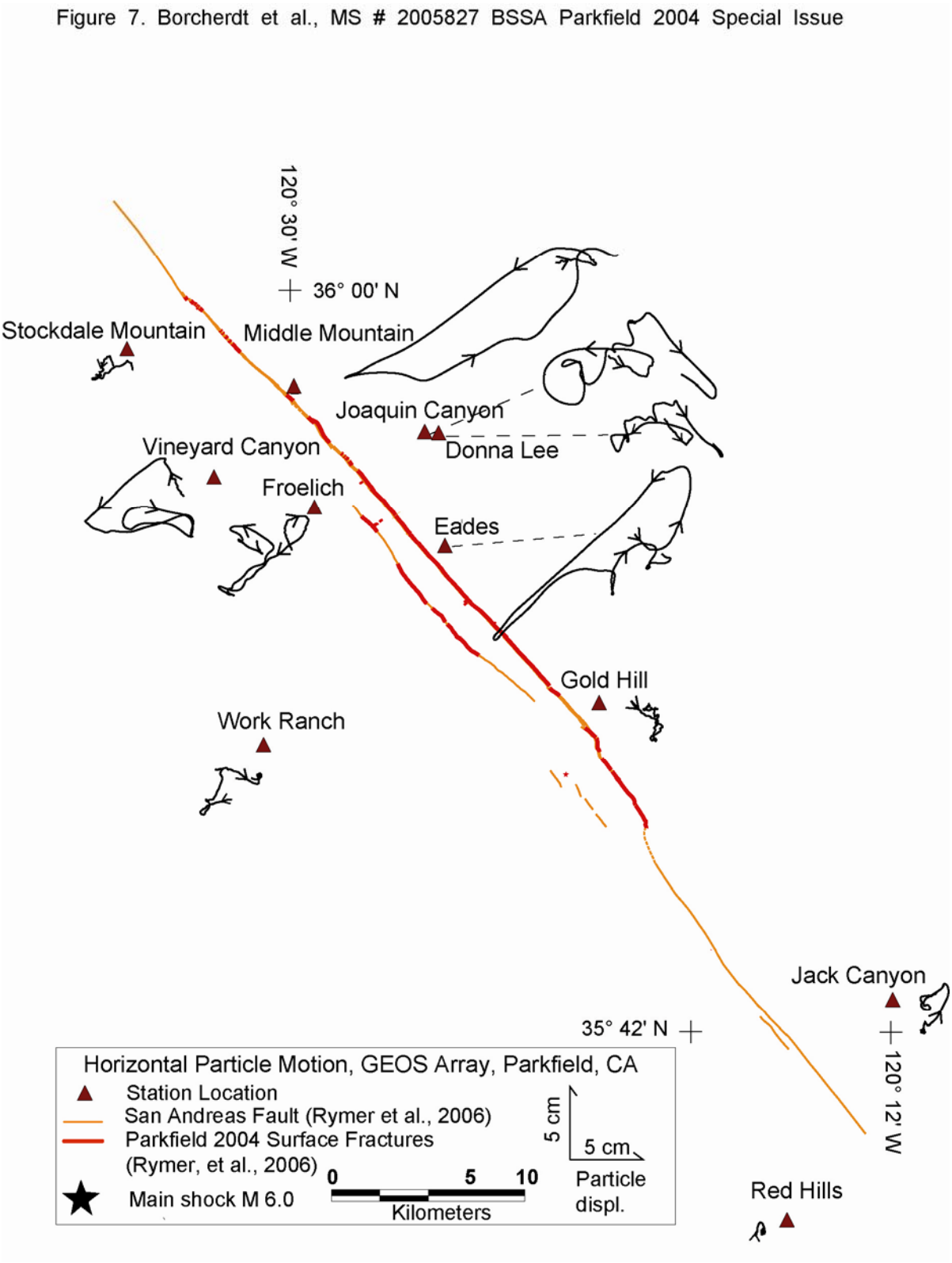

Figure 8. Borcherdt et al., MS # 2005827 BSSA Parkfield 2004 Special Issue

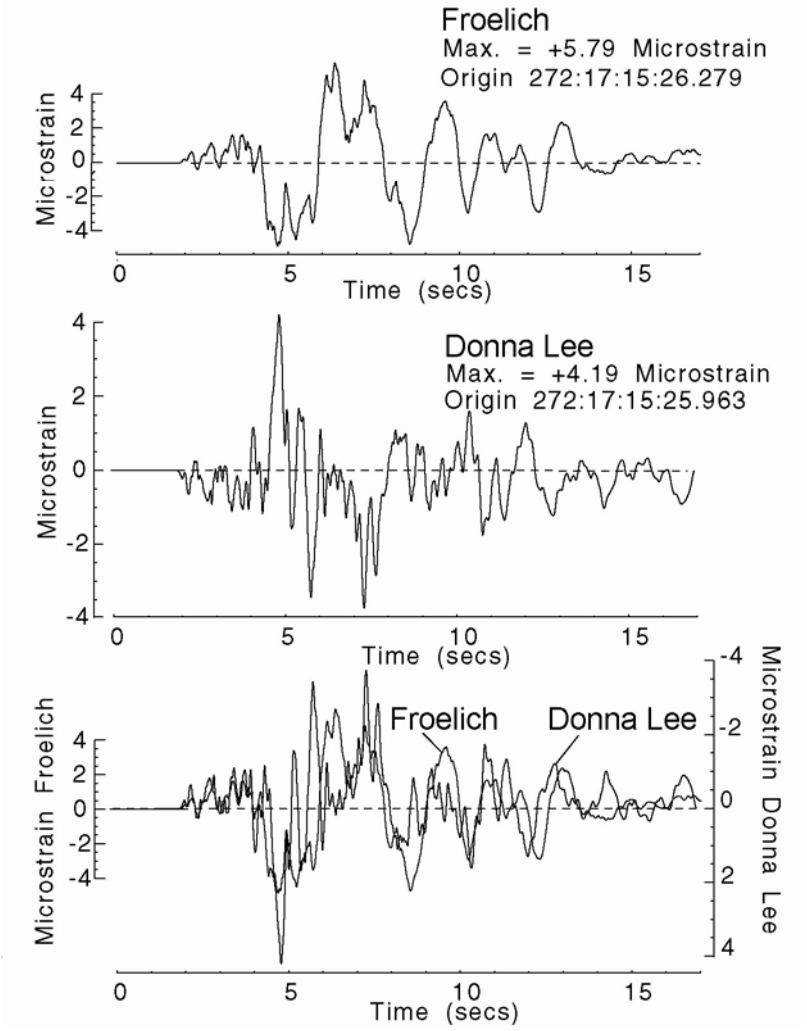

Figure 9. Borcherdt et al., MS # 2005827 BSSA Parkfield 2004 Special Issue

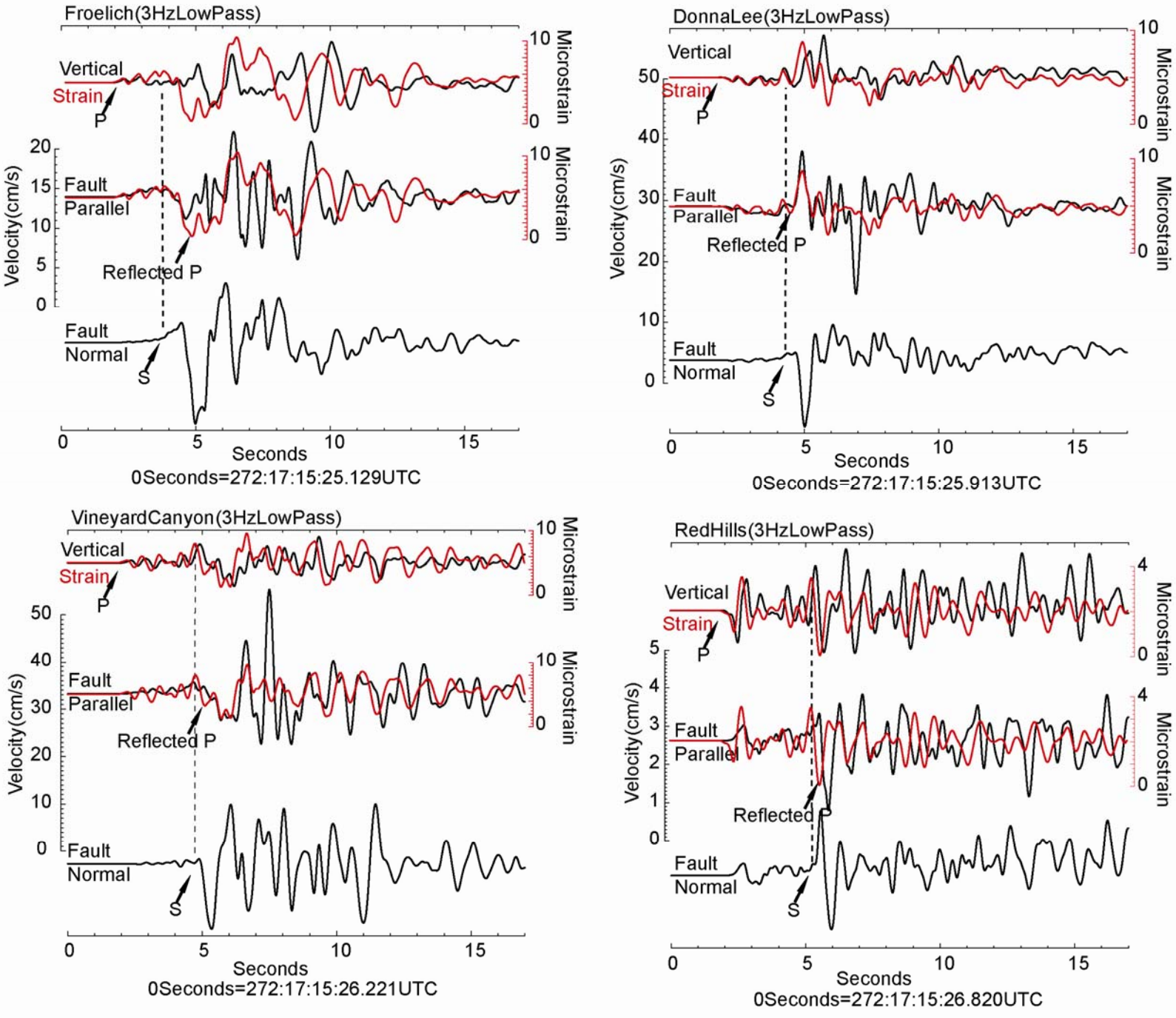

Figure 10. Borcherdt et al., MS # 2005827 BSSA Parkfield 2004 Special Issue